

Article

Smart Graphene Nanoplatelet Strain Sensor for Natural Frequency Sensing of Stainless Steel (SS304) and Human Health Monitoring

Debadatta Sethy *  and Krishnan Balasubramaniam 

Center for Non-Destructive Evaluation, Indian Institute of Technology Madras, Chennai 600036, India; balas@iitm.ac.in

* Correspondence: debadatta6@gmail.com

Abstract: The main purpose of this article is to monitor the natural frequency of stainless steel (SS304) with and without defect by spray-coated smart graphene nanoplatelet (GNPs)-doped poly (methyl methacrylate) (PMMA) nanocomposite strain sensor and human health by smart Lycra denim textile sensor. Methods such as impact hammer test and NI-daq, finite element method (FEM) simulation by Abaqus 6.12, and fast Fourier transform (FFT) study were applied for frequency monitoring of SS304. For human health monitoring, edema disease inspection, cough, and biceps locomotion were studied by graphene sol-gel textile sensor. We report eight sensors fabricated by scotch tape exfoliation method and their sensitivity was checked in terms of gauge factor (GF). The highest and lowest GF-based sensors were checked for sensitivity in the defect (hole) specimen. These sensors were used to sense the natural frequency of SS304 at three different positions in the cantilever beam. The same quantity of GNPs was used for making Lycra denim textile sensors for human health monitoring. The Lycra denim textile sensor showed a 216% change in resistance in the left calf muscle, which is less than right leg flexibility, indicating good sensitivity. In addition, the textile sensor helped in sensing coughing and biceps monitoring. The ease in fabrication and high sensitivity demonstrate the potential ability of GNPs for futuristic smart material for structural and human health monitoring.

Keywords: graphene nanoplatelets; Lycra textile sensor; spectroscopical characterization; frequency response function; modal shapes



Citation: Sethy, D.; Balasubramaniam, K. Smart Graphene Nanoplatelet Strain Sensor for Natural Frequency Sensing of Stainless Steel (SS304) and Human Health Monitoring. *Materials* **2022**, *15*, 3924. <https://doi.org/10.3390/ma15113924>

Academic Editor: Francesco Iacoviello

Received: 20 March 2022

Accepted: 22 April 2022

Published: 31 May 2022

Publisher's Note: MDPI stays neutral with regard to jurisdictional claims in published maps and institutional affiliations.



Copyright: © 2022 by the authors. Licensee MDPI, Basel, Switzerland. This article is an open access article distributed under the terms and conditions of the Creative Commons Attribution (CC BY) license (<https://creativecommons.org/licenses/by/4.0/>).

1. Introduction

Stainless steel of grade SS304 is one of the most versatile widely used stainless steels, having excellent forming and welding characteristics. It is excellent in a range of environments and many corrosive media. SS304 is also resistant to warm chloride environments and to stress corrosion cracking above 60 °C. It also has good weldability by all standard fusion methods both with and without filler metals. Therefore, because of these properties, SS304 has versatile applications in plates and pipelines. It has a lot of applications in beer brewing, milk processing, and winemaking equipment. From kitchen, benches, sinks, troughs equipment, and appliances to architectural paneling, railings, and trim, SS304 is a promising tool for many usages. In thermal power plants, and also mining areas, SS304 is used basically for heat exchangers, woven screens, quarrying, and water filtration, respectively. Even in mechanical devices, such as threaded fasteners and springs, SS304 has contributed a lot. Therefore, its inspection is of high concern for the industry. In advance non-destructive (NDT) techniques such as infrared (IR) thermography, ultrasonic testing, computed tomography (CT), spectroscopy analysis, etc., are used for the inspection of stainless steel. However, these techniques are excellent but not reliable, and have a high maintenance cost. Therefore, to avoid these maintenance costs and poor reliability, a smart sensor made from GNPs is the best solution. Graphene nanoplatelet, being a 2D material, is the derived form of graphite. It reflects the allotrope form of carbon-containing numerous

double bonds having an electronic configuration of [He] $2s^2 2p^2$ situated at the p-block in the periodic table. Each atom in a graphene sheet is connected to its three nearest neighbors by a σ -bond and contributes one electron to a conduction band that extends over the whole sheet. This rearrangement of structure and electronic configuration helps in sensing the outer environment. GNP is a crystalline form of the element carbon with its atom arranged in a hexagonal structure. In addition, properties such as high mobility charge carriers, monoatomic thickness, and high surface area help in sensing the health monitoring of structures [1–5]. Graphene has its unique properties due to its electronic band structure which plays a vital role in electronic and optoelectronic devices. This helps in studying the tunable work function. This tunable study has demanded much attention towards graphene usage in the modern era [6]. Graphene has not only limited itself to optoelectronic properties but also can attenuate electromagnetic pollution. It also has good shielding properties because of its structure that helps in transmission loss of the incident electromagnetic wave [7]. Many health monitoring works have been carried out on structures and the human body with graphene [8–12]. Here, in this article, graphene has been suspended over substrate polymethyl methacrylate (PMMA), which is an amorphous and thermoplastic polymer that maintains good hardness and strength in making sensors. In addition, GNPs enhance the microstructure and viscoelastic characteristics of PMMA. Smart sensors, especially made from graphene materials as substrates, have been studied [13–15]. Substrates such as PMMA have been studied as reinforcement carbonaceous filler for obtaining well-dispersed alignment-based nanocomposites with GNP. Many graphene-doped PMMA sensors for human health monitoring have been reported from heart rate, pulse oxygenation, blood glucose meter, to electrocardiogram signal, etc., by novel monitoring devices made out of graphene [16]. In addition, thermal management work taking graphene as a sensing indicator has been studied in which PMMA acts as a substrate in GNPs-based nanocomposite sensors [17,18]. In our previous work, the thermal signature was improved by making PMMA a substrate by doping graphene into it. Much structural health monitoring work has been reported by GNP sensors in which excellent GF obtained has been deployed in thermal imaging and also in strain monitoring activity [19–22]. The graphene-based sensor is also best for piezoresistive sensing which has been proved in many works such as energy harvesting and beam sensing purposes [23,24]. These sensors are brittle but show good response in electromechanical coupling. To overcome the brittleness, many graphene-doped functionalized sensors have been implemented in sensing [25]. Some functionalized materials such as polydimethylsiloxane, and also reduced form of graphene, help not only in high sensitivity but are also capable of proximity sensing capability [26–28]. Graphene, being a smart material, has tremendous application not only in piezoelectric response limited to beams but also in textiles, too. Much work has been carried out for finding the natural frequency of graphene platelets but it has not been implemented as a sensor for sensing the natural frequency of structures in terms of piezoresistivity.

Many works have also been carried out, such as silk spandex fabric strain sensor by coating reduced graphene oxide in which performance was measured by performing a cyclic test which remained constant for 1000 cycles [29]. Even some interesting work in gait monitoring has also been reported, where the knee region was monitored by two identical sensors made out of graphene [30]. In the medical field, online data monitoring had been performed on patients for asymmetrical walkway motion, but here it is very costly in sensor installation, which was a photoelectric beam, and also a time cost factor [31]. Many works such as laser-induced graphene have been implemented on the skin for motion monitoring. This is a laser direct writing process whose power consumption and installation cost are too high. Some graphene Ecoflex sandwich structures have been implemented for vocal fold vibration detection purposes where the drop-casting method was used for the production of the sensors [32].

The main objective is to monitor the natural frequency of SS304 in defect (1 mm diameter hole) and without-defect specimens by spray-coating the structure and to monitor human health by sol-gel-coated Lycra denim sensor. Therefore, the article has been divided

into three parts; the first one is regarding experiments with an impact hammer for natural frequency calculation with the help of NI-USB daq-4432, and then we study the sensing behavior with GNPs/PMMA sensor. The second is regarding surface modeling to study the modal analysis affecting the resistance behavior during natural frequency sensing. Then, a sol-gel coated graphene sensor is used for studying human body locomotion and edema disease analysis.

2. Sensor (GNPs/PMMA) Fabrication

In the fabrication, as shown in Figure 1, of a smart GNPs/PMMA sensor, three chemicals were taken, namely, GNPs of 50 mg (thickness < 2–4 nm; lateral size = 5 μm , received generously from GRAPHENE LAB Ltd., London, UK) were mixed with THF-AR of 100 mL. Then the solution was sonicated for 10 h. Similarly, a solution of PMMA of 2 mg and THF of 20 mL was sonicated for 4 h and then both the solutions were mixed and sonicated for more than 8 h. After sonication, the GNP sensor was ready for fabrication upon SS304. The GNP sensor then was spray-coated and a scotch tape was used for mechanical cleavage to maintain the intrinsic electrical resistance, as shown above in Figure 1f. Therefore, overall, eight GNP spray-coated sensors upon SS304 were fabricated and were mechanically cleaved to maintain intrinsic resistances such as 200 Ω , 400 Ω , 500 Ω , 650 Ω , 800 Ω , 900 Ω , 1 k Ω , and 3.5 k Ω . These sensors were further tested for sensitivity analysis compared with an industrial strain gauge (HBM1-LY41-6/350 ($R_0 = 0.35$ k Ω ; measured GF is ~ 1.6)).

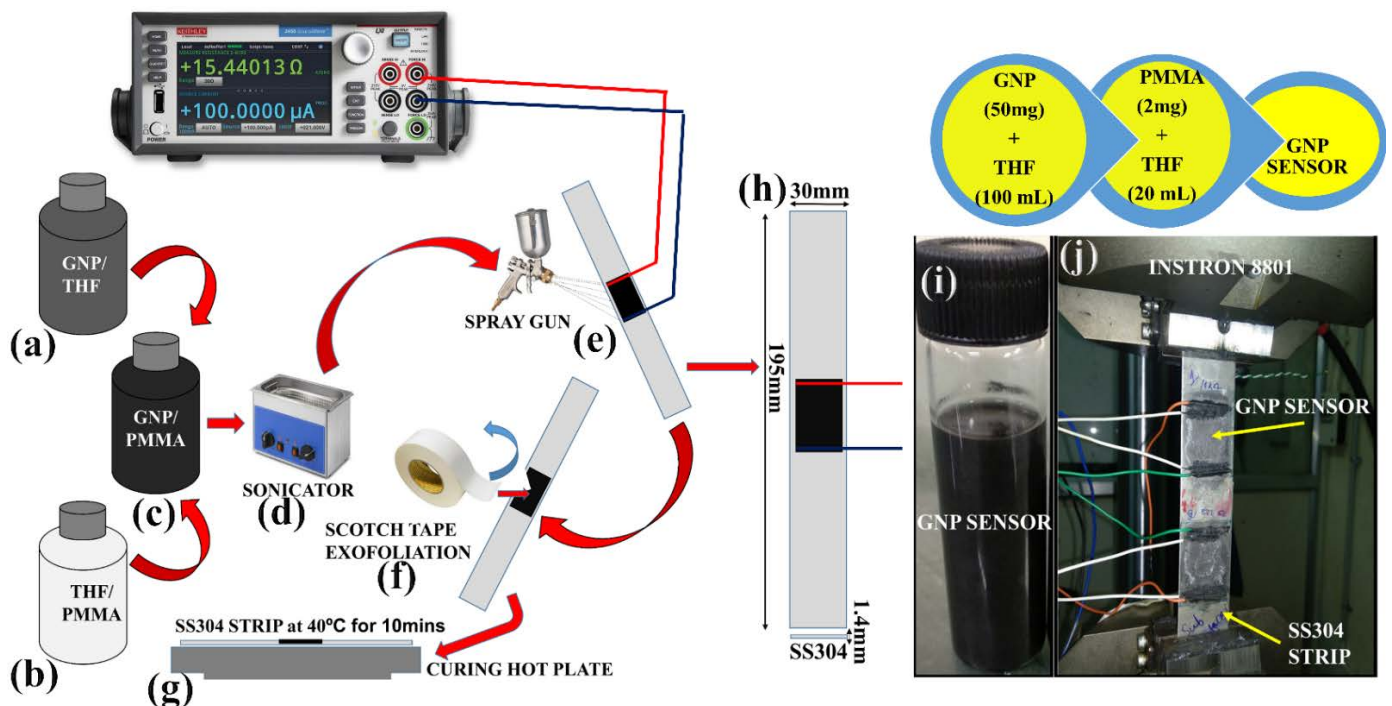


Figure 1. Experimental setup for smart GNPs/PMMA sensor: (a–g) Sensor preparation from ultrasonication to spray-coating approach upon SS304 specimen; (h) SS304 specimen with geometrical dimensions (195 mm \times 30 mm \times 1.143 mm); (i,j) GNPs/PMMA spray-coated sensor for sensitivity test upon SS304 by UTM INSTRON (8801).

3. Characterization

As shown in the above Figure 2, for characterization, XRD analysis was performed for both pure GNPs, pure PMMA, and GNPs/PMMA/THF. This is the most comprehensive study and characterization to identify unknown materials and is relatively reliable for identifying the structure and composition of any material from the position in terms of degree and intensities of diffraction peak. From the above figure, it is observed that the position of the XRD peak, which correlates to the powder film platelets behavior of

GNPs material, falls at the value of 2θ at 26° . This indicates the presence of GNPs in our raw material, whose microstructure can be visualized from the SEM image as shown in Figure 2b. These GNPs' (thickness < 2–4 nm; lateral size = 5 μm , received generously from GRAPHENE LAB Ltd., London, UK) properties can be seen in Figure 2c. Similarly, in Figure 2d, XRD was performed also for PMMA and PMMA/GNPs/THF solution. It shows the presence of metha-acrylate, which has three intensity peaks, one at 13.6° another at 23° , and one at 42.6° , which describes the amorphous nature of PMMA. The sensor solution (GNPs/PMMA/THF) also shows the intensity peak because of the presence of PMMA, GNPs, and THF. The narrow peak observed in Figure 2d falling at 25° and 30.6° show the good crystallinity of PMMA. In addition, Figure 2e,f show the morphology of PMMA and GNPs/PMMA. Here, in the PMMA morphology, the crystalline lamellae structure is separated from the amorphous phase, which makes PMMA turn black under SEM [33]. Similarly, GNPs are also doped into PMMA, which can be seen as flakes of sheets on the surface of PMMA. Here, PMMA is acting as the substrate which holds GNPs on it that acts as a smart nanocomposite sensor.

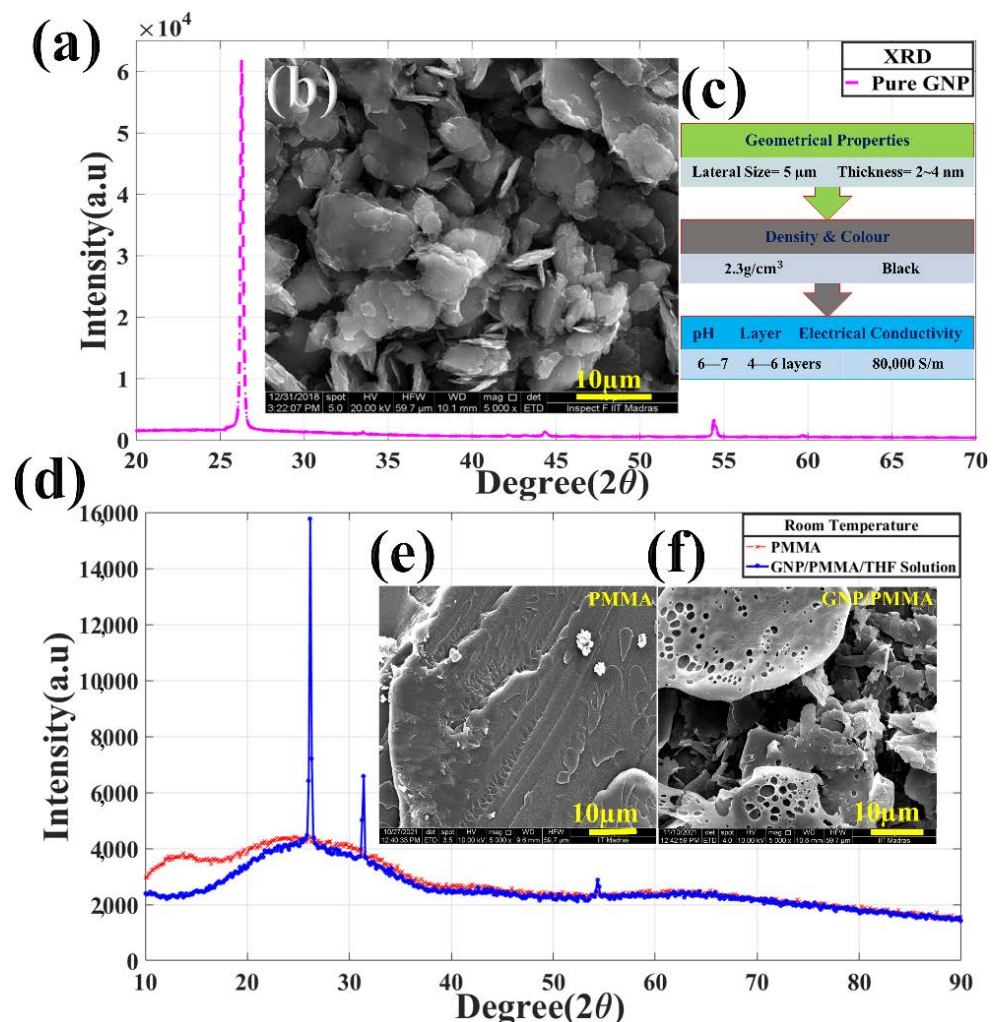


Figure 2. Experimental setup for thermal monitoring during tensile loading: (a) XRD of pure GNPs; (b) SEM image of GNPs; (c) properties of GNPs bought from (GRAPHENE LAB Ltd., London, UK); (d) XRD of pure PMMA and GNP/PMMA/THF solution; (e,f) SEM image of PMMA and PMMA-doped GNPs.

4. Experimental Setup

In the experimental setup, as shown in Figure 3, the arrangement was performed for both sensitivity analysis of strain gauge and GNPs/PMMA sensor. These smart sensors

were first tested upon Instron-8801 UTM under uniaxial loading at the rate of 1 mm/min at strain-controlled loading, which can be seen in Figure 1j. As shown from Figure 3a, National Instruments-based LabVIEW (version 2016, CNDE Lab, IIT-Madras, Chennai, India) software is interfaced with NI-DAQ USB-4432 for data collection at the sampling frequency of 1000, and correspondingly, a Keithley SourceMeter-2450 was used for resistance data collection. In Figure 3b,c, an impact hammer (DYTRAN_DYNAPULSE, Chatsworth, CA, USA) is shown and it is attached with a BNC coaxial connector to USB-4432 at one end and the accelerometer is connected to the other end of the USB-4432. Figure 3d,e shows the smart sensor from GNPs/PMMA and industrial strain gauge fabricated upon SS304, which senses the change in resistance during natural frequency excitation.

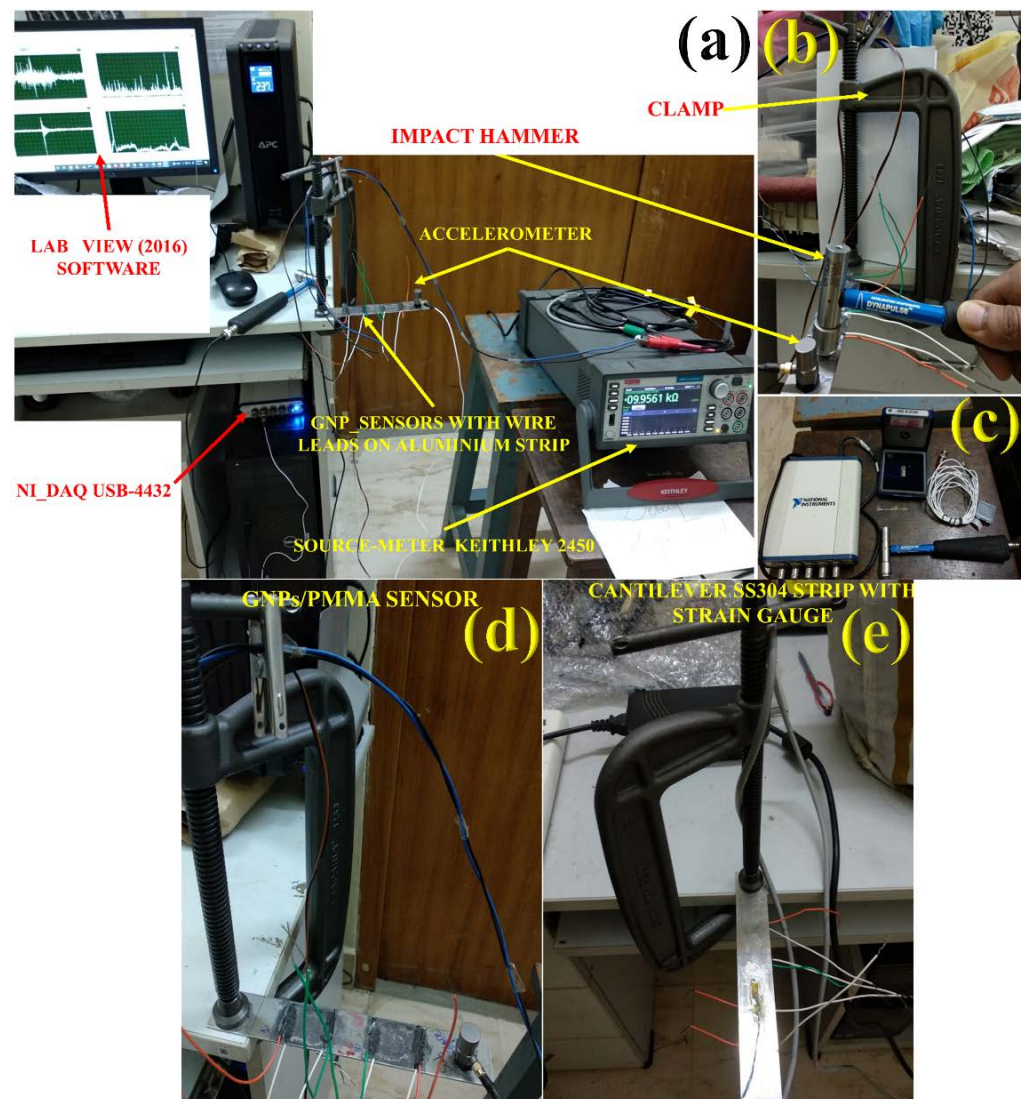


Figure 3. Experimental setup for natural frequency calculation of SS304 strip: (a) LabVIEW (2016) software and NI-DAQ USB-4432 used for natural frequency calculation with Keithley SourceMeter-2450 for electrical resistance calculation; (b) clamp being used for fixing SS304 strip with accelerometer and impact hammer; (c) electronic gadgets for impact hammer method (DAQ USB-4432), wax for fixing accelerometer, cable chords for accelerometer and impact hammer; (d) GNPs/PMMA sensor fabricated and accelerometer fixed upon SS304; (e) industrial strain gauge fixed to SS304 for comparative study.

5. Results and Discussion

5.1. Natural Frequency Sensing of SS304

As shown in the above Figure 4a,b, first of all, eight specimens were spray-coated with the GNPs/PMMA-based sensor. Then, these sensors were exfoliated mechanically by scotch tape, as already explained in Figure 1. Then, these sensors were brought under intrinsic resistances of 200 Ω, 400 Ω, 500 Ω, 650 Ω, 800 Ω, 900 Ω, 1 kΩ, and 3.5 kΩ, and these sensors were checked then for sensitivity analysis against an industrial strain gauge (350 Ω).

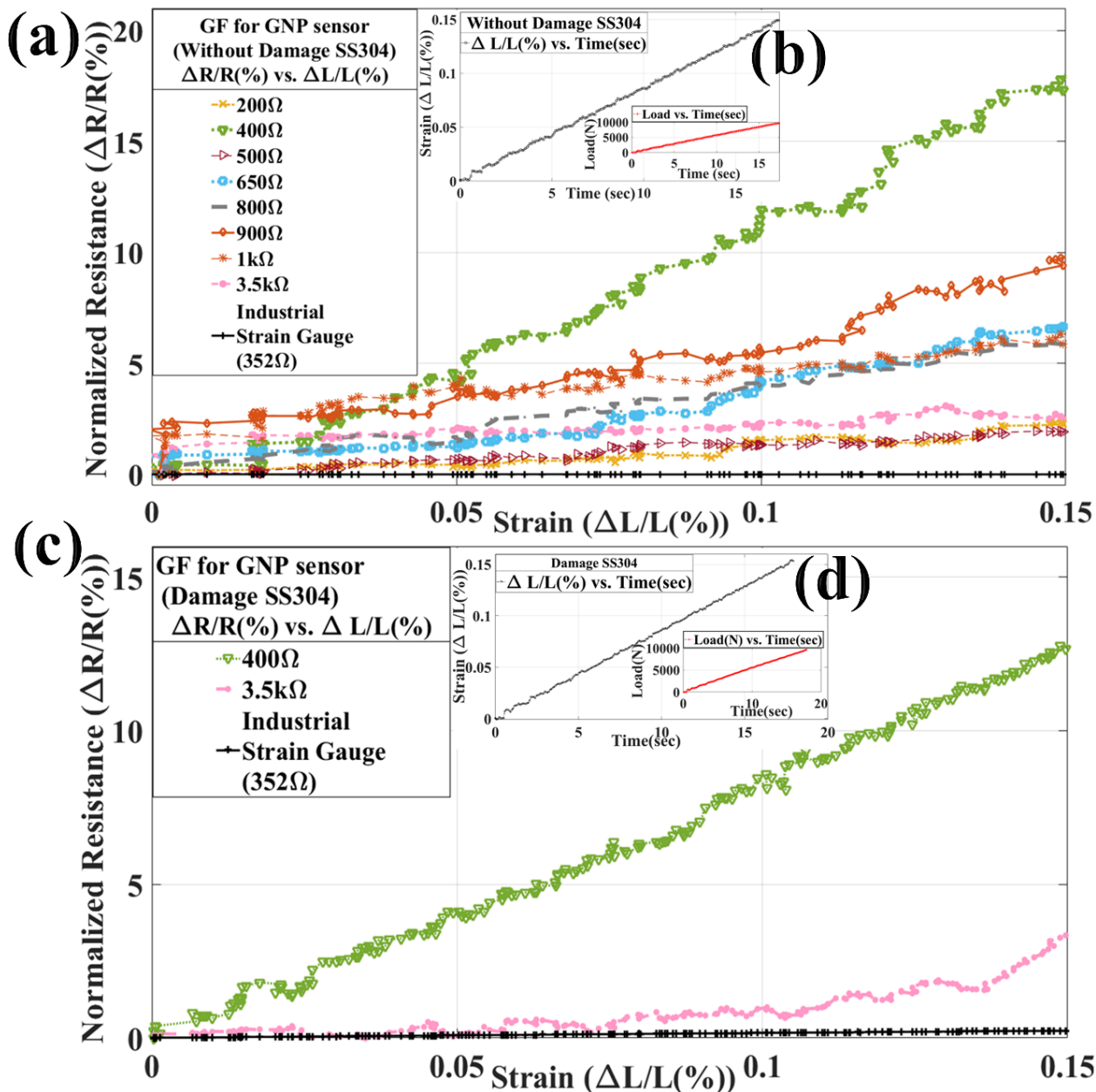


Figure 4. Graph showing gauge factor (GF) with defect and without-defect SS304 specimen: (a,b) GF calculation by GNPs/PMMA sensor without-defect specimen SS304 and corresponding strain data with respect to time, respectively; (c,d) GF calculation from highest and lowest GF GNPs/PMMA sensor with defect (hole) specimen SS304 and corresponding strain data with respect to time.

Here, sensitivity is checked under piezoresistivity action in terms of gauge factor (GF). GF is a parameter that correlates electrical resistance with the mechanical strain which is expressed always as

$$\text{Sensitivity (GF)} = \frac{\frac{\Delta R}{R} \%}{\frac{\Delta L}{L} \%} \quad (1)$$

Here, $\frac{\Delta R}{R} \%$ is the normalized resistance and $\frac{\Delta L}{L} \%$ is the normalized strain. These embedded sensors upon SS304 were tested at UTM Instron-8801 under monotonic load conditions at a crosshead displacement rate of 1 mm/min within the elastic range of SS304.

As observed from Figure 4a,b, the GF for 200 Ω, 400 Ω, 500 Ω, 650 Ω, 800 Ω, 900 Ω, 1 kΩ, and 3.5 kΩ are 52, 263, 36, 141, 84, 116, 65, and 25, respectively. The maximum strain achieved during uniaxial loading within elastic range was 0.15% for 18 s and load of 9500N. These GNPs/PMMA sensors have higher sensitivity than that of industrial strain gauge of 350 Ω, which is 1.5. Now, as the strain increases, the electrical resistance also increases, and hence GF becomes high. As shown in Figure 4c,d, the highest and lowest GF obtained from Figure 4a underwent sensitivity analysis for defect (1 mm diameter hole) based on SS304. The GF obtained from uniaxial loading is 86, 16, and 0.64 for 3.5 kΩ, 400 Ω, and industrial strain gauge, respectively. These higher and lower GF are further used for sensing impact hammer testing during natural frequency finding of a SS304 strip, as shown in Figure 5.

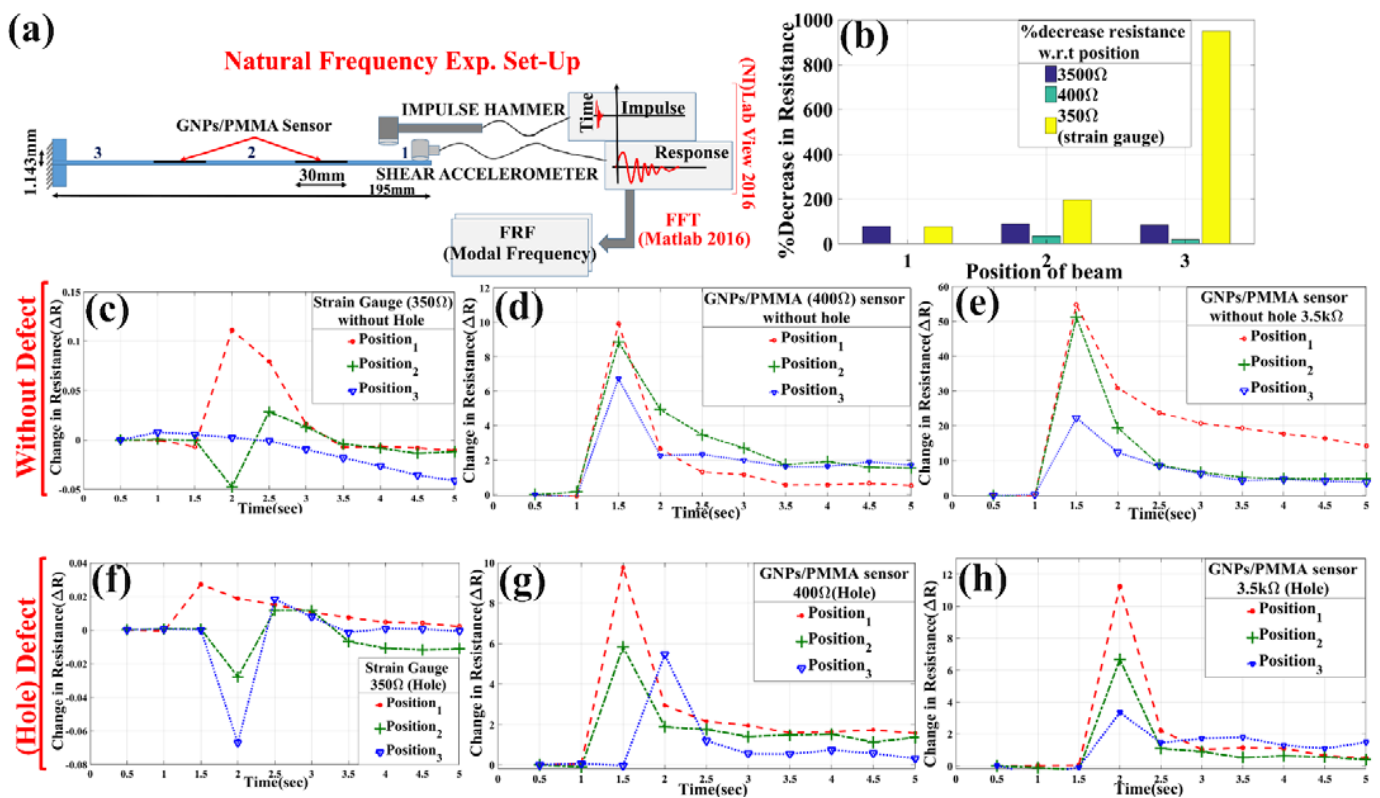


Figure 5. Experimental setup for finding natural frequency: (a) Impulse hammer and shear accelerometer used for natural frequency finding with attached GNPs/PMMA sensor; (b) histogram showing % decrease of resistance from hole specimen by sensors; (c–e) change in electrical resistance by industrial strain gauge, 400 Ω and 3.5 kΩ GNPs/PMMA sensor at without-defect SS304; (f–h) change in electrical resistance by industrial strain gauge, 400 Ω and 3.5 kΩ GNPs/PMMA sensor at with (hole) defect SS304.

As shown in Figure 5a, the SS304 strip is fixed to one end by a clamp, and 3.5 kΩ, 400 Ω, and strain gauge (350 Ω) are fixed at a distance of 15 mm from the mid-center of the specimen on the hole (defect) and without-defect specimen. These are used on the specimen to find peak amplitude (resistance) at the respective position of impact hammering. In the

experiment, impact hammer (DYTRAN) and shear accelerometer are used for impulse and response behavior with respect to time by interfacing NI-DAQ LabVIEW 2016 for obtaining data at the sampling frequency of 1000. Then, the impact hammer was tapped (perturbed) upon both the defect and without-defect specimen, and the Keithley SourceMeter-2450 (Tektronix, Beaverton, OR, USA) was used for resistance data collection. Then, force data and acceleration data were used for modal frequency calculation by taking FFT in terms of frequency response function (FRF) from Matlab 2016. After processing the data, natural frequencies were found in terms of resistance change, as shown in Figure 5c–h. It is observed from Figure 5, from without-defect specimen, that the sensing of the amplitude of resistance peak varies with varying of deflection during tapping with an impact hammer. For strain gauge (350 Ω), the highest peak of resistance amplitude was found to be at the free end at position 1, as shown in Figure 5a. At positions 1, 2, and 3, the peak resistance changes of the strain gauge rose to 0.115 Ω , 0.02844 Ω , and 0.007904 Ω , respectively, for without defect, as observed in Figure 5c. Similarly, for the defect sample, as seen from Figure 5f, the peak resistance dropped down to 0.02713 Ω , -0.0278 Ω , and -0.06711 Ω , respectively, for positions 1, 2, and 3. Therefore, the % decrease in resistance of the defect specimen from without-defect specimen fell to 76.4%, 197.74%, and 949.06%, respectively, whereas when sensed with GNPs/PMMA sensor of 400 Ω , it was found that for the without-defect specimen, as seen from Figure 5d, at positions 1, 2, and 3, the peak rose to 9.927 Ω , 8.859 Ω , and 6.738 Ω . For the defect specimen, as observed from Figure 5g, the peak rose to 9.761 Ω , 5.832 Ω , and 5.455 Ω . Therefore, the % decrease of resistance from without defect to defect fell to 1.67%, 34.16%, and 19.04%, respectively, corresponding to positions 1, 2, and 3. Similarly, for 3.5 k Ω , as observed in Figure 5e,h, the resistance decreased down to 11.23 Ω , 6.672 Ω , and 3.343 Ω from 54.81 Ω , 51.16 Ω , and 22.26 Ω with the % decrement of 79.511%, 89.9586%, and 84.982%, respectively. This % decrement of resistance can be well observed from the histogram shown in Figure 5b and quantitative data analyzed in Table 1.

Table 1. Quantitative analysis of electrical resistance during impact hammering at different positions.

Gauge Factor with Resistance	Position of Impact Hammering (Natural Frequency)	Without Defect ($\Delta R(\Omega)$)	With Defect (Hole) ($\Delta R(\Omega)$)	% Decrease in Resistance Change ($\Delta R\%$)	Difference in Resistance Change ($\Delta R(\Omega)$)
3.5 k Ω	1	54.81	11.23	79.511	−43.58
	2	51.16	6.672	89.9586	−44.488
	3	22.26	3.343	84.982	−18.917
400 Ω	1	9.927	9.761	1.672207	−0.166
	2	8.859	5.832	34.16	−3.027
	3	6.738	5.455	19.04126	−1.283
350 Ω _Industrial strain gauge	1	0.115	0.02713	76.40	−0.08787
	2	0.02844	−0.0278	197.7496	−0.05624
	3	0.007904	−0.06711	949.064	−0.075014

To understand the interface mechanism, a simulation study was carried out on Abaqus software 6.12 for finding the natural frequency. The natural frequency (f_n) is obtained from the Euler–Bernoulli equation of cantilever fixed-free thin beam [34,35], generally defined as the below equation:

$$\frac{\partial^4 y}{\partial x^4} + \left(\frac{\rho A}{EI}\right) \frac{\partial^2 y}{\partial t^2} = 0 \quad (2)$$

From the above fourth-order equation, mass (m) = ρA (density \times area) and the natural frequency (f_n) are defined as the frequency at which a system tends to oscillate in the absence of any driving or damping force, and is expressed mathematically as

$$f_n = \frac{C_i^2}{2\pi} \sqrt{\frac{EI}{mL^4}} \quad (3)$$

where E is the Young's modulus of the SS304 strip, I is the moment of inertia, m is the mass of SS304, L is the length of specimen, and C_i is the mode of vibration. The values of the mode of vibration are expressed below:

$$C_i = \beta_i L = 1.875, 4.694, 7.85, 11 \dots \dots \dots \text{etc.} \quad (4)$$

Correspondingly, FRF was analyzed without-defect specimen and with defect (hole) specimen after finding FFT from acceleration vs. time data. As shown in Figure 6b, at position 1 (free end), the impact hammering was performed with a force of 20.32N with an acceleration of 14.6 m/s² and, finally, it was reduced down logarithmically. In addition, for the frequency values obtained, as seen from Figure 6a, the modest frequency peak was found to be in the region 21.4 Hz following the next mode with a magnitude of 33.8 Hz. The third mode was found to be 157.2 Hz and the fourth mode was 189.8 Hz. The fifth mode was found to be 258 Hz and the sixth mode was 301.8 Hz. The force amplitudes for corresponding modes are found to be 0.02703N, 0.0333N, 0.02088N, 0.04014N, 0.0452N, and 0.4137N, after performing FFT. Similarly, for position 2, the impact hammering was performed with 8.141 N force and acceleration of 20.92 m/s², as shown in Figure 6d. The first mode was found to be at 28.4 Hz following the second mode at 126.8 Hz. The third, fourth, fifth, and sixth were found to be 160.4 Hz, 175.6 Hz, 191 Hz, and 210.6 Hz, respectively. The corresponding force amplitudes were 0.0371N, 0.044N, 0.05667N, 0.0329N, 0.0328N, and 0.05519N. In addition, third hammering was performed at position 3 near the fixed end. As seen in Figure 6e,f, the specimen was excited with a force at 8.559N and acceleration of 2.486 m/s². The natural frequencies for modes first, second, third, fourth, fifth, and sixth are 29.8 Hz, 50.4 Hz, 67.2 Hz, 166 Hz, 189.2 Hz, and 217.8 Hz. The corresponding force values for the modes are 0.01303N, 0.03925N, 0.06108N, 0.03337N, 0.0353N, and 0.05745N. Hence, it is observed that the natural frequencies value increases with an increase in force value. Similarly, the experiment was performed for defect (hole) specimens.

As observed in Figure 7a,b, the maximum force is reached at 13.46N and slowly reduced down to -7.989N. Then, the force is reduced down to 6.543N to -1433N in the next decrement cycle, and slowly down to 2.181 N in a decrement manner. Therefore, the acceleration is also retarded slowly from 14.18 m/s² to -33.58 m/s², and consecutively the acceleration is retarded further down to 6.178 m/s². Then it came down further to 3.794 m/s² and then to 3.103 m/s², and came near to rest after logarithmic decrement in the further displacement down to 0.84 m/s².

In the FFT study between the acceleration and frequency, the frequency was found from the FRF graph obtained as shown in Figure 7a,b. The modest peak amplitude is observed at a frequency of 24.6 Hz, the next peak is observed at 32.8 Hz, and the third peak is at 84 Hz. Similarly, frequencies at higher-order modes were observed at 109 Hz, 133.2 Hz, and 157.6 Hz for fourth, fifth, and sixth respectively. As seen from the force vs. frequency graph, it is observed that the corresponding frequencies increase with increment of force amplitude at 0.023N, 0.01781N, 0.06472N, 0.0605N, 0.1745N, and 0.053N. Similarly, for position 2, as seen in Figure 7c,d, the force is reduced from 5.076N to 7.081N and correspondingly the acceleration is retarded down from 14.94 m/s² to 3.176 m/s², and slowly the retardation of the cycle reached 0.292 m/s². The corresponding frequency obtained from modes of vibration at first mode is at 33.4 Hz, following the second order frequency at 50.4 Hz. The corresponding frequencies at higher order modes are 67.2 Hz, 146 Hz, 173 Hz, and 184.2 Hz. The modest peak is observed at a frequency of 146 Hz and 173 Hz during the time of impact hammering. When the corresponding FFT data

between force and frequency are plotted, it is found that the force function is increased vs. frequencies. The force amplitudes are 0.1173N, 0.05745 N, 0.09897N, 0.09117N, 0.02483N, and 0.04178N. Similarly, for position 3, as seen in Figure 7e,f, the force and acceleration values are 16.97N and 1.825 m/s^2 , respectively. After performing FFT of acceleration and frequency, the frequency values obtained are 33.6 Hz, 49 Hz, 86.8 Hz, 132.8 Hz, 209 Hz, and 250.6 Hz, respectively, for first, second, third, fourth, fifth, and sixth modes. Similarly, the force amplitudes also increase with the increment of frequencies. For the first, second, third, fourth, fifth, and sixth modes of vibration, the corresponding force amplitudes after FFT are 0.0576N, 0.05195N, 0.06883N, 0.06543N, 0.0879N, and 0.09497N.

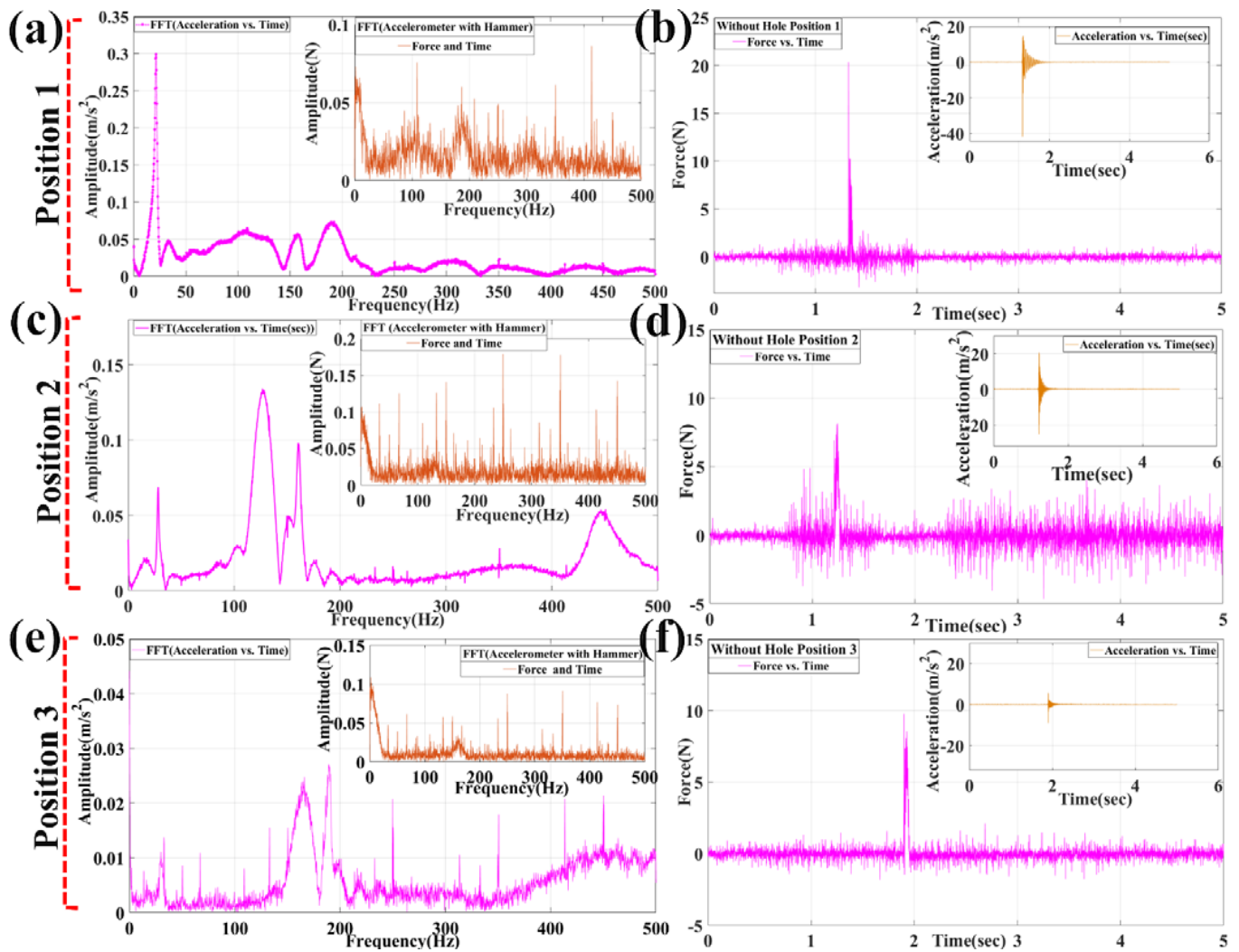


Figure 6. FFT graph plotted by MATLAB 2016 for obtaining modes of frequencies from acceleration and force amplitude with respect to time and its corresponding magnitude graphs at different positions of impact hammering (without hole): (a,b) FFT graphs and magnitude graphs for acceleration and force for position 1; (c,d) FFT graphs and magnitude graphs for acceleration and force for position 2; (e,f) FFT graphs and magnitude graphs for acceleration and force for position 3.

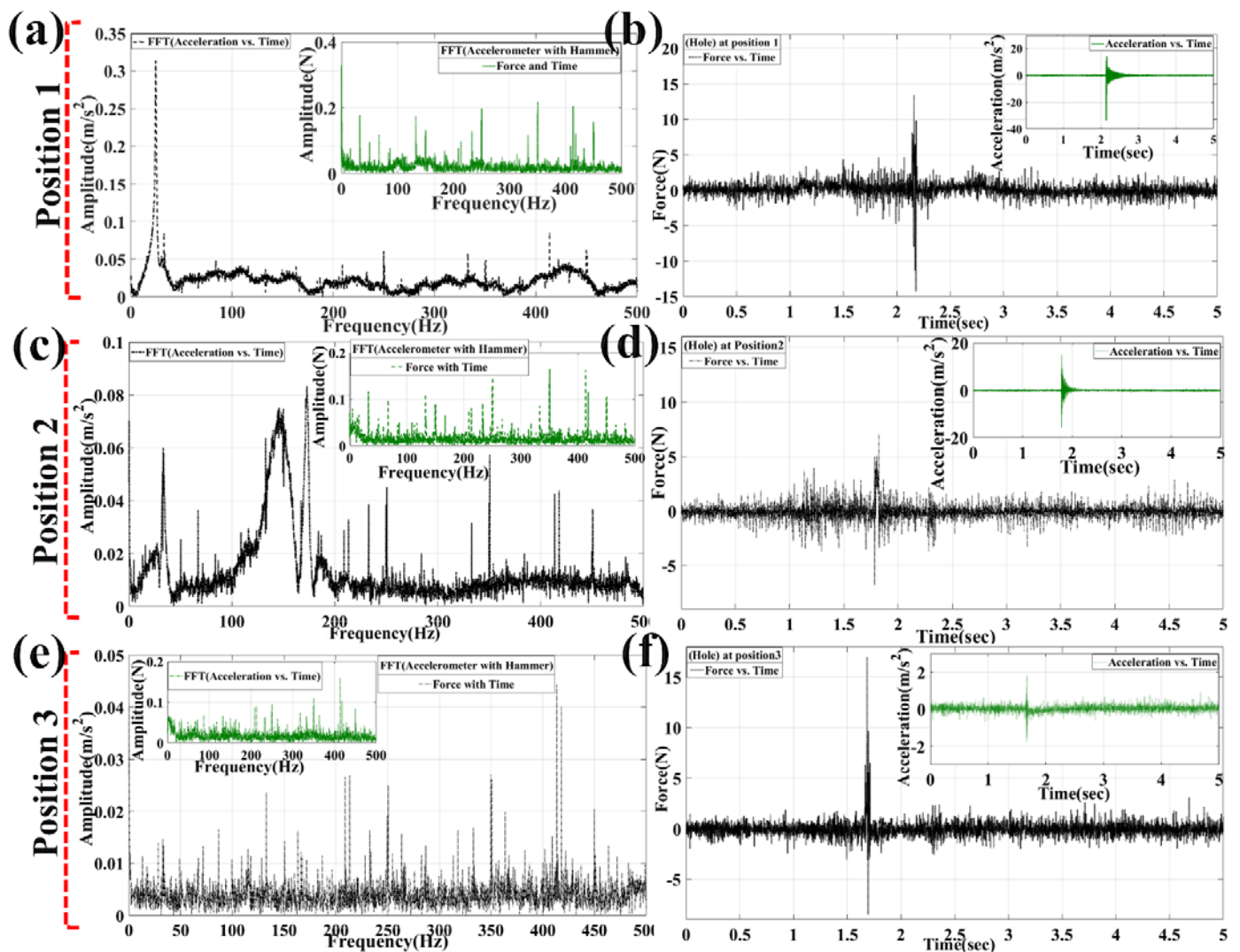


Figure 7. FFT graph plotted by MATLAB 2016 for obtaining modes of frequencies from acceleration and force amplitude with respect to time and its corresponding magnitude graphs at different positions of impact hammering (with (hole) defect): (a,b) FFT graphs and magnitude graphs for acceleration and force for position 1; (c,d) FFT graphs and magnitude graphs for acceleration and force for position 2; (e,f) FFT graphs and magnitude graphs for acceleration and force for position 3.

As seen in Figure 8a,b, mode shapes have been shown. Here, 2D and 3D mode shapes are shown for specimens without defects. Here, the mode shapes are of different shapes, as can be seen from simulation modeling by Abaqus 6.12. In mode 1, the shape is similar to an extension and for mode 2, skin surface went down, making a compressive pattern in mode shapes. Hence, piezo action comes into play and the GNPs/PMMA sensor gives output in terms of change in resistance, as already explained in Figure 5. Similarly, in mode 3, mode 4, mode 5 and mode 6, frequencies are higher as compared to mode 1 and mode 2. The graphene-based sensor is highly sensitive to the beam's bending action. Therefore, the modes in the beam's vibration lead to a change in resistance. These modes make the GNPs particle disoriented, and resistance changes from the initial value to a higher range with modes of vibration. Similarly, in the case of the specimen with a defect (hole), the sensitivity of the GNPs/PMMA sensor is reduced to a lower % decrease in resistance, as explained above in Figure 5. The % increase of resistance is more for the without-defect specimen as compared to the defect (hole) one.

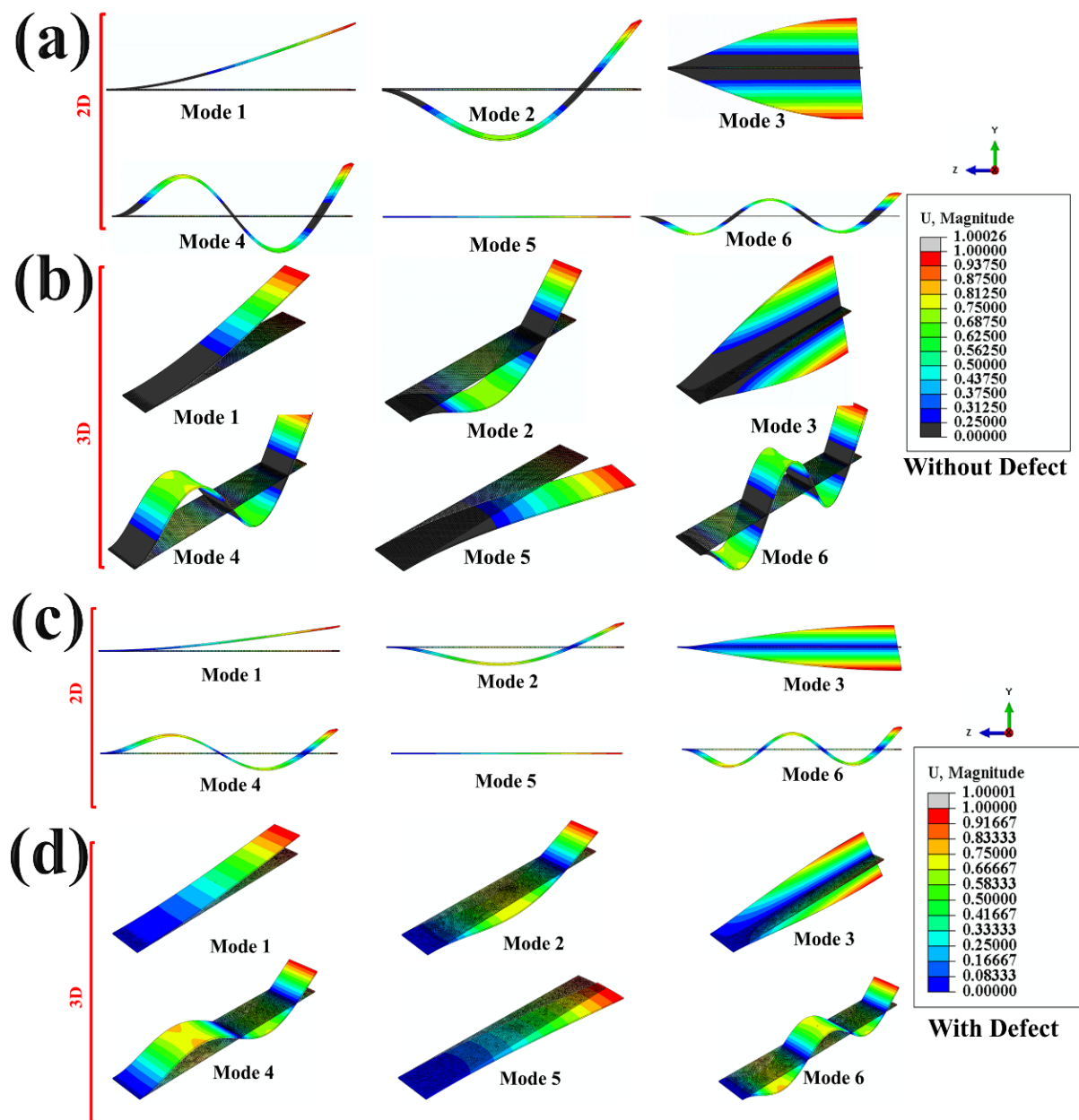


Figure 8. Modal shapes obtained through FEM (Abaqus 6.12) simulation. (a,b) 2D and 3D mode shapes of all frequencies for without defect (hole); (c,d) 2D and 3D mode shapes of all frequencies with defect (hole).

5.2. Human Health Monitoring

Here, GNPs are coated with Lycra denim textiles by sol–gel solutions. First of all, Lycra denim textile of ASTM D-5035 was cut into pieces of dimension 150 mm × 30 mm. Then, the Lycra denim textile was rinsed with running water for 5 min. Then it is dried and after drying it was purified again with ethanol by dipping it for 1 h. This completes the cleansing action by anhydrous ethanol. Then, graphene nanoplatelets of 100 mg weight were added to a beaker and 300 mg of sodium lauryl sulfate (SDS) was added. Then, the beaker was set for 3 h under ultrasonic homogenizer at 200 W with 30% amplitude at a frequency of 50 Hz. This helps in the dispersion of GNPs with SDS. Hence, this completes the action of a dispersing agent. Then, in an Erlenmeyer flask, a separate solution for organo-silicon sol was prepared. This is the process for reagent preparation in which 37.28 gm of diethoxydimethyl silane (DEDMS) was poured into 53 mL of 2% aq. solution of polyvinyl alcohol (PVA). Then, 0.28 mL of aluminum isopropoxide mixed with isopropanol

(0.015 mol/L) was added and the solution was kept for 2 h at room temperature. After 2 h, the reagent solution was then mixed with 0.8 gm of tetraethoxysilane (TEOS) and 4.1 gm of 3-glycidoxypropyl triethoxysilane (GPS) was added to it. Then the whole solution was mixed with dispersing agent solution.

Then, the solution was set for 8 h under a magnetic stirrer. Then, after 8 h, the Lycra denim textile cloth was dipped into it and was left for 1 h to be coated completely. Then, the cloth was taken out and was washed under running water. Then, the sol-gel coated textile was dried, and hence the smart sensor Lycra denim textile was ready for experimentation. This can be well observed in Figure 9a–c. Here, basically the smart textile's main objective is to develop a wearable textile that can sense the movement of the biceps, throat, and calf muscles of the leg in the human body. The biceps brachii muscle is one of the chief muscles of the arm whose origin is at the scapula and insertion into the radius of the biceps. Therefore, this itself comes into play between the shoulder joint and the elbow joint. This locomotion in the forearm make the bicep between joints perform flexion and supination action that brings tensile and compressive action in the mechanical sense [36–38]. Therefore, this compressive action and tensile action in the forearm makes the biceps develop piezoaction on the surface of the Lycra denim smart textile sensor. The output is obtained in terms of piezoresistive signals that are collected with the Keithley SourceMeter. The spandex-based wrapped cotton Lycra denim cloth was prepared according to ASTM-D5035 standard having a length of 150 mm, a width of 30 mm, and the gauge length of 95 mm, as shown in Figure 10f, and then lead wires were attached with silver paste, as can be seen from Figure 10g. As seen in the above Figure 10a–c, SEM images were taken for sol-gel-coated smart textile at 500 μm , 500 μm , and 100 μm , respectively. The sol-gel GNPs-based Lycra denim textile sensor senses in terms of change in electrical resistance during piezoresistive action. The smart textile sensor, having an intrinsic resistance of 23 M Ω after using the same wt% of GNPs that was 50 mg, was used for textile sensor fabrication. As seen in Figure 10d,e, EDAX was performed from SEM analysis to know the carbon (C%) and oxygen (O%) after sol-gel coating which were found to be 47.9% and 52.15%, respectively. Then, the textile sensor was tested for sensitivity analysis, as shown in Figure 10h,i. The smart textile sensor underwent sensitivity analysis by Instron (8801) at the displacement rate of 1 mm/min, 2 mm/min, and 3 mm/min, as shown in Figure 10l–n. The GF, as mentioned in Equation (1), for the Lycra textile sensor, was found to be 1.5, which had repeatability at 2 mm/min and 3 mm/min strain testing. This can be well observed in Figure 10k. First of all, three Lycra denim textiles of ASTM-D5035 were cut and tested for tensile strength till the break at a different displacement rate of 1 mm/min, 2 mm/min, and 3 mm/min. At 1 mm/min, the load reached 8.13N at 1136s up to the elastic limit, and then after crossing the plastic deformation, reached breakpoint load at 398N at 2860 s, and then the cloth was torn due to elastane breakage in between the fibers. Similarly, at 2 mm/min of displacement rate, elastic limit reached 4N at 398 s, which then, after crossing plastic deformation, reached breakpoint load of 310N at 1123 s and then elastane fibers were ruptured, and for the displacement rate of 3 mm/min, the load at the elastic point is 6.68N at 230 s which, later after plastic deformation, reached breakpoint load of 347.8N at 715 s.

Correspondingly, the tensile extension up to an elastic point for 1 mm/min was 8.606 mm at 8.606 s. Similarly, for 2 mm/min and 3 mm/min, the tensile extension was 13.61 mm at 13.61 s and 17.98 mm at 17.98 s, respectively. In each case of strain testing, the tensile strength was found to be the same, that is, 10.245 MPa with ultimate tensile strength (UTS), as 13.27 MPa, as shown in Figure 10i. Therefore, the sensitivity analysis was performed in the linear zone all within the range of the elastic zone. Here, GF was found to be the same as 2.5 in the linear region slope of tensile extension with 8.606 mm, 13.6 mm, and 17.98 mm for 1 mm/min, 2 mm/min, and 3 mm/min, respectively, as shown in Figure 10k. During tensile extension of Lycra denim textile, the elastane fibers inside the cotton wrap stretch and lose their elasticity once it crosses the elastic limit, and plastic deformation leads to tensile failure of the Lycra textile fabric, as shown in

Figure 10l–n. Here, at spots 1, 2, and 3, as seen, the fabrics are ruptured and gaps can be seen, signifying the failure of elasticity. Therefore, the sensing of Lycra denim should be achieved within its elasticity limit. This smart Lycra denim textile sensor in this article has been explained for sensing physiological locomotion in the biceps, neck, and leg calf muscle in edema conditions.

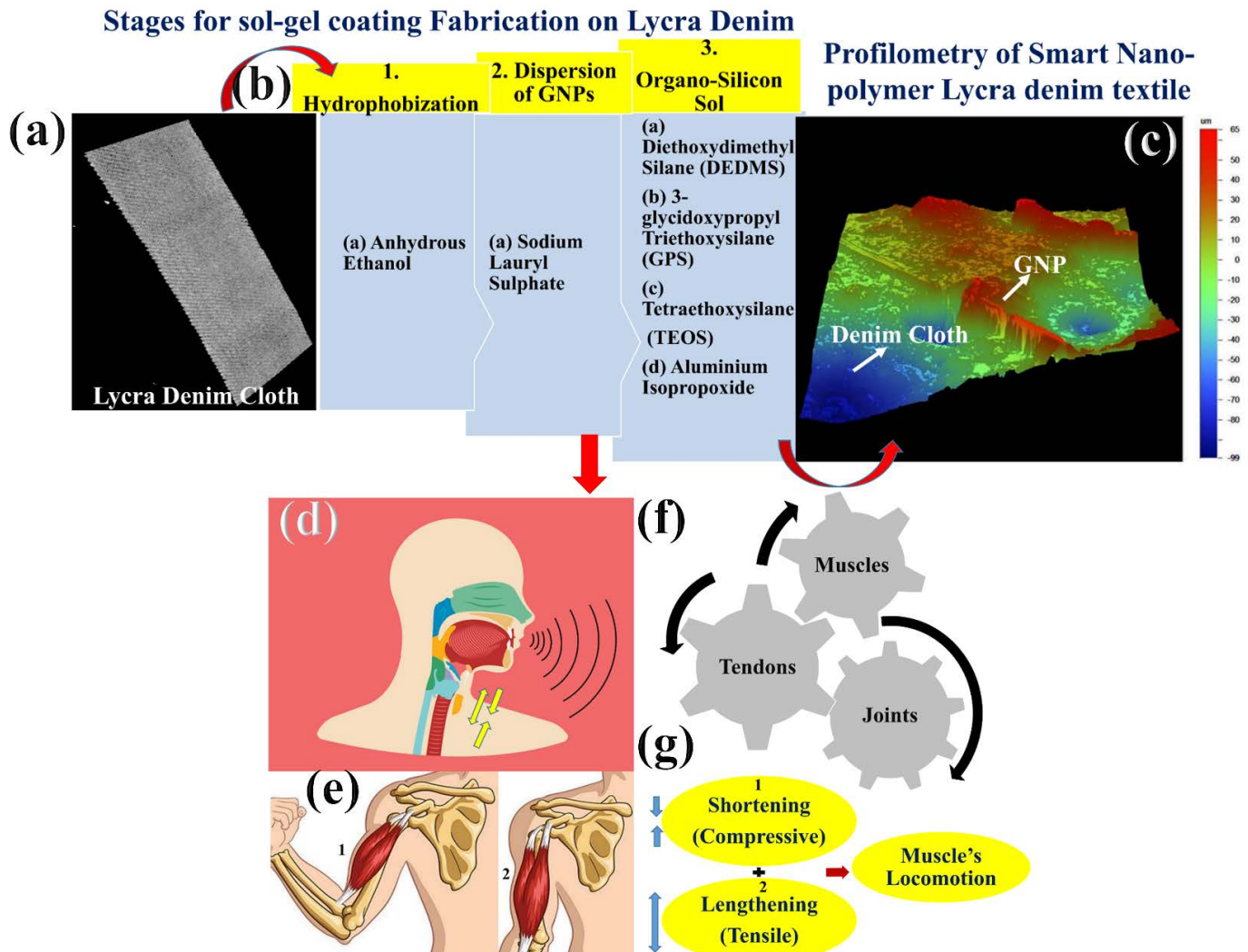


Figure 9. Fabrication of smart Lycra denim textile cloth and profilometry study: (a,b) computed tomography of Lycra denim cloth and b chemicals used for sol–gel coating fabrication upon Lycra denim textile; (c) profilometry used for measurement of thickness of coating; (d,e) sensor location for wrapping around neck and bicep zone; (f,g) schematic for human body locomotion with muscles, tendons, and joints during compressive and tensile action.

Edema is a disease that is water retention being trapped under muscles in the human body, which can be seen in Figure 11c,d. It is a type of swelling caused by excessive fluid trapped in our body's tissues. It is the bridge between capillary filtration (lymph formation) and lymphatic drainage. If lymph formation exceeds lymphatic drainage due to either increment of capillary filtration and non-uniformity of lymphatic flow, it leads to raising of venous pressure [39,40]. This, later on, causes venous obstruction as a clot. The consequences of edema lead to calf pain and difficulty in walking. The locomotion in the calf muscle is governed by three parameters, namely, muscle, tendons, and joints. These all together lead to the shortening and lengthening of muscle fibers. Hence, the concentric and eccentric mechanism starts from regular standing to standing on tiptoes and lowering heels slowly back to the floor from tiptoes, respectively. The gastrocnemius and soleus muscles

taper and merge at the base of the calf muscle called the Achilles tendon. This tendon helps in stretching the calf muscle, and on relaxing, tends to bring back the muscle to its original position. This repetition of tensile-compressive nature in the calf muscle leads to fatigue cycle, which is sensed by GNPs sol-gel smart-coated textile. Here, the sensor has been employed at the top of the edema region.

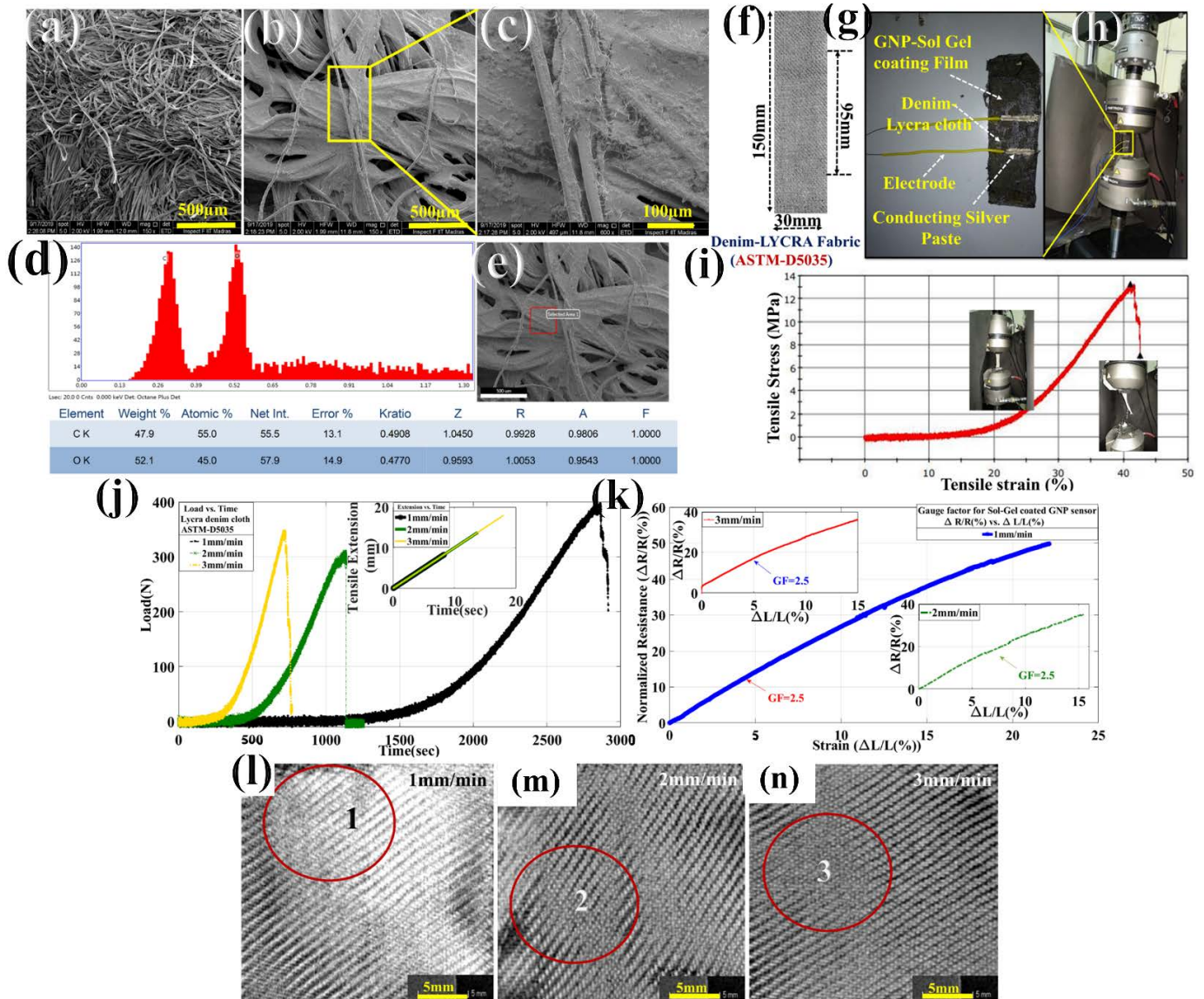


Figure 10. SEM study and sensitivity analysis of smart sol-gel-coated Lycra denim textile sensor: (a–c) SEM image taken at 500 μm and 100 μm; (d,e) EDAX for elemental mapping; (f–i) ASTM D5035-based Lycra denim textile for sensitivity testing under INSTRON-8801; (j) load and extension data with respect to time; (k) sensitivity test at different displacement rate; (l–n) CT image testing at different displacement rates.

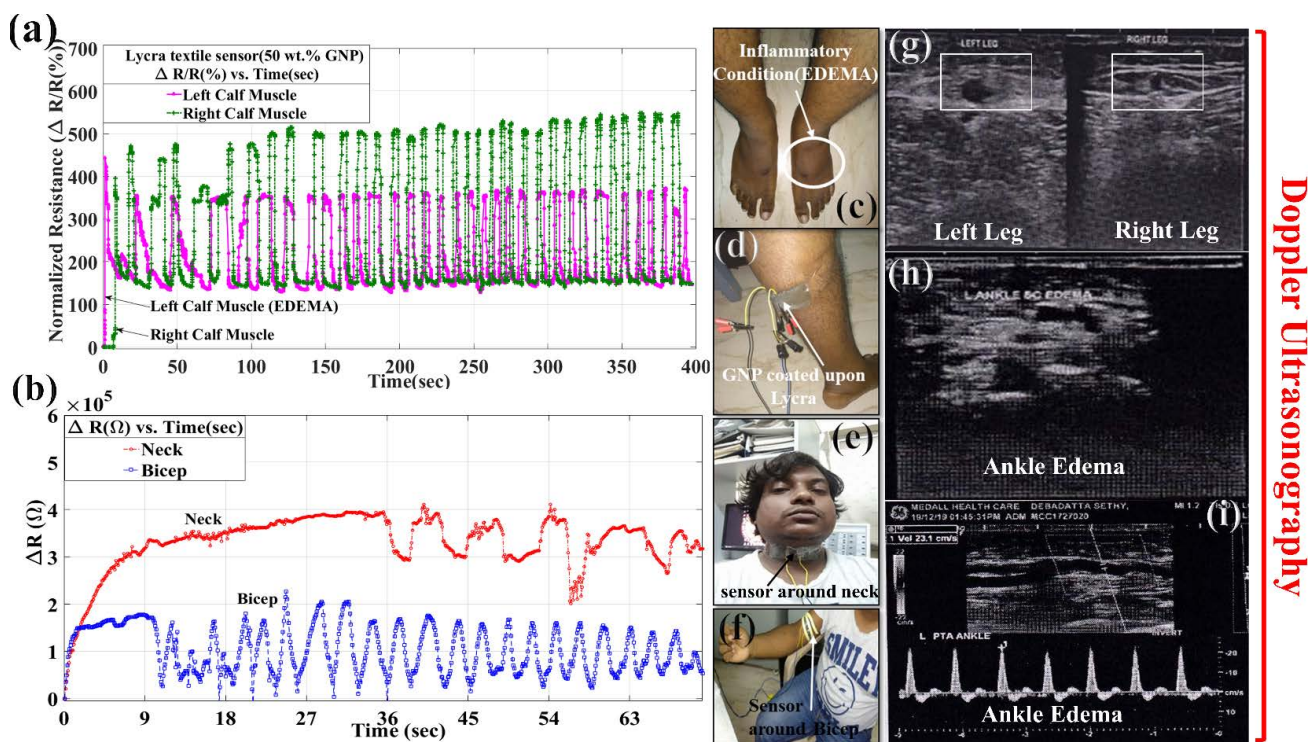


Figure 11. Experimental setup for electrical resistance data analysis by wearable Lycra denim sensor coated with GNPs and sol-gel solutions: (a) Normalized resistance change at left and right calf muscles for edema detection by smart Lycra textile sensor (coated with GNPs and sol-gel solutions); (b) change in resistance for neck and biceps detected by smart Lycra textile sensor (coated with GNPs and sol-gel solutions); (c–f) inflammation showing edema at ankle, Lycra textile sensor attached at calf muscle, neck, and biceps, respectively; (g–i) Doppler ultrasonography for confirmation of EDEMA.

The flexibility of both the legs was checked with electrical resistance data collected from the Lycra sensor with the Keithley SourceMeter during piezoresistance action, as shown in Figure 11a. This graph shows the sensitivity of the edema condition in terms of piezoresistive action. The cycle in the graph is tensile–tensile, in which 34 cycles were played in stretching each leg and bringing it down to its original position for 400 s. The normalized resistance change in baseline shifting was followed by 145.5% during cycling loading in leg locomotion from both the legs. Here, the peak rise of amplitude in terms of normalized resistance is very low in the case of the left leg (361.5% from baseline shifting), but for the right leg, the peak rise in normalized resistance is 520.6%. This delayed rise in the peak of normalized resistance monitors the structural health of the calf muscle, which again was verified with Doppler ultrasonography, as shown in Figure 11g–i. It is an imaging technique that uses sound waves to show blood moving through blood vessels. Therefore, it works by measuring sound waves that are reflected from moving objects such as red blood cells. This is known as the Doppler effect [41]. In Figure 11g, there is a big lumped circular black spot mass in the standing condition which shows blockage in blood flow which is absent in the right leg. As shown in Figure 11h, the ankle also shows a lot of spots blocking the blood flow path. The arteries of the left lower limb show a little swollen appearance of the artery walls. Minimal subcutaneous edema is seen from the left leg and foot, but the appearance is mildly hyperechoic compared to the right calf region. Therefore, the superficial venous system appears mildly prominent in the left lower limb. Few incompetent perforators are seen in the medial and posterior aspects of the leg. Therefore, there is a possibility of mild inflammatory changes. This indicates that image analysis matches with normalized resistance that leads to confirmation of our GNPs-based Lycra textile sensor in sensing the edema. As shown in Figure 11b, for the

bicep, the change in resistance amplitude rose to $1.64 \times 10^5 \Omega$ from the baseline shifting of $2.499 \times 10^4 \Omega$. For 20 cycles of testing in the biceps, the piezoresistive action between the sensor and bicep muscle leads to a change in resistance in cyclic loading in the biceps. Similarly, the sensitivity was checked for the throat region during coughing, in which the change in resistance shifted from a baseline of $2.932 \times 10^5 \Omega$ to $4.109 \times 10^5 \Omega$, and it was repeated for two cycles. Here, coughing condition was not uniform because of irregularity in larynx motion and the surface of the textile sensor. For the third cyclic behavior at 54 s, it tended to rise at the same amplitude as first cyclic loading, that is, to $4.109 \times 10^5 \Omega$, but it fell to $2.016 \times 10^5 \Omega$ due to irregularity in locomotion of the larynx. It rose again after 60 s, and again it rose to $3.651 \times 10^5 \Omega$, and the cycle of coughing ended after falling from $3.54 \times 10^5 \Omega$ to $3.092 \times 10^5 \Omega$. This is shown in Figure 11e,f.

6. Conclusions

Therefore, it is concluded that the sensitivity in the case of the GNPs-doped PMMA strain sensor during natural frequency varies with impact hammering at different positions. We observed that the % decrease in resistance for the GNPs/PMMA sensor of 3.5 k Ω and 400 Ω is relatively low, which is the relative difference between the defect and without-defect specimen, but in case of industrial strain gauge, the % decrease in resistance is more, compared to 3.5 k Ω and 400 Ω . In the case of smart denim textile sensors, the sensing ability of sol-gel-coated GNP textile with the same wt% of GNPs helps in sensing edema, neck, and bicep locomotion. The locomotion of left and right calf muscles were sensed for edema disease confirmation. In this, the left leg locomotion showed less peak in amplitude change than the right calf muscle. The left leg locomotion was monitored with 216% amplitude normalized, whereas in the right leg, it was 375.1% amplitude. The left leg had less locomotion, which was verified with Doppler ultrasonography, and in the neck, the peak rising and falling was detected with fall of amplitude as $4.109 \times 10^5 \Omega$, $3.651 \times 10^5 \Omega$, and $3.54 \times 10^5 \Omega$ gradually, with a decrement of larynx movement. In addition, the bicep locomotion was also monitored successfully in every tensile stretching of muscle fibers. Therefore, it is experimentally proven that the GNP-based sensor acts as a promising indicator for health monitoring not only of SS304, but also of human health monitoring.

Author Contributions: Both authors contributed to the study conception and design. Material preparation, data collection, and analysis were performed by D.S. Experimental support provided by K.B. The first draft of the manuscript was written by D.S. and both authors commented on previous versions of the manuscript. Conceptualization, review, and editing were performed by K.B. All authors have read and agreed to the published version of the manuscript.

Funding: This research did not receive any specific grant from funding agencies in the public, commercial, or not-for-profit sector. No funding was received to assist with the preparation of this manuscript. This work is part of the author's PhD work.

Institutional Review Board Statement: Not applicable.

Informed Consent Statement: Both authors agree to submit this article to Materials: MDPI. The case study during health monitoring was performed upon author of correspondence.

Data Availability Statement: Not applicable.

Conflicts of Interest: The authors declare no conflict of interest. The authors declare that they have no known competing financial interests or personal relationships that could have appeared to influence the work reported in this paper.

References

1. Yan, T.; Wang, Z.; Pan, Z.J. Flexible strain sensors fabricated using carbon-based nanomaterials: A Review. *Curr. Opin. Solid State Mater. Sci.* **2018**, *22*, 213–228. [[CrossRef](#)]
2. Lee, J.H.; Lee, K.Y.; Gupta, M.K.; Kim, T.Y.; Lee, D.Y.; Oh, J.; Ryu, C.; Yoo, W.J.; Kang, C.Y.; Yoon, S.J.; et al. Highly Stretchable Piezoelectric-Pyroelectric Hybrid Nanogenerator. *Adv. Mater.* **2013**, *26*, 765–769. [[CrossRef](#)] [[PubMed](#)]

3. Bae, S.H.; Lee, Y.; Sharma, B.K.; Lee, H.J.; Kim, J.H.; Ahn, J.H. Graphene-based transparent strain sensor. *Carbon* **2013**, *51*, 236–242. [[CrossRef](#)]
4. Wang, Y.; Wang, L.; Yang, T.; Li, X.; Zang, X.; Zhu, M.; Wang, K.; Wu, D.; Zhu, H. Wearable and Highly Sensitive Graphene Strain Sensors for Human Motion Monitoring. *Adv. Funct. Mater.* **2014**, *24*, 4666–4670. [[CrossRef](#)]
5. Chen, S.; Wei, Y.; Yuan, X.; Lin, Y.; Liu, L. A highly stretchable strain sensor based on a graphene/silver nanoparticle synergic conductive network and a sandwich structure. *J. Mater. Chem. C* **2016**, *19*, 4304–4311. [[CrossRef](#)]
6. Naghdi, S.; Sanchez, A.G.; Rhee, K.Y. Tuning the work function of graphene toward application as anode and cathode. *J. Alloys Compd.* **2019**, *805*, 1117–1134. [[CrossRef](#)]
7. Naghdi, S.; Jaleh, B.; Eslamipناه, M.; Moradi, A.; Abdollahi, M.; Einali, N.; Rhee, K.Y. Graphene family, and their hybrid structures for electromagnetic interference shielding applications: Recent trends and prospects. *J. Alloys Compd.* **2022**, *900*, 163176. [[CrossRef](#)]
8. Tolvanen, J.; Hannu, J.; Jantunen, H. Stretchable and Washable Strain Sensor Based on Cracking Structure for Human Motion Monitoring. *Sci. Rep.* **2018**, *8*, 13241. [[CrossRef](#)]
9. Liu, Z.; Qi, D.; Guo, P.; Liu, Y.; Zhu, B.; Yang, H.; Liu, Y.; Li, B.; Zhang, C.; Yu, J.; et al. Thickness-Gradient Films for High Gauge Factor Stretchable Strain Sensors. *Adv. Mater.* **2015**, *27*, 6230–6237. [[CrossRef](#)]
10. Liu, X.; Tang, C.; Du, X.; Xiong, S.; Xi, S.; Shen, X.; Zheng, Q.; Wang, Z.; Wu, Y.; et al. A highly sensitive graphene woven fabric strain sensor for wearable wireless musical instruments. *Mater. Horiz.* **2017**, *4*, 477–486. [[CrossRef](#)]
11. Choi, D.Y.; Kim, M.H.; Oh, Y.S.; Jung, S.H.; Jung, H.J.; Sung, H.J.; Lee, H.W.; Lee, H.M. Highly Stretchable, Hysteresis-Free Ionic Liquid-Based Strain Sensor for Precise Human Motion Monitoring. *ACS Appl. Mater. Interfaces* **2017**, *9*, 1770–1780. [[CrossRef](#)]
12. Huang, Y.; Gao, L.; Zhao, Y.; Guo, X.; Liu, C.; Liu, P. Highly flexible fabric strain sensor based on graphene nanoplatelet–polyaniline nanocomposites for human gesture recognition. *J. Appl. Polym. Sci.* **2017**, *134*, 45340. [[CrossRef](#)]
13. Kausar, A. Emerging trends in poly (methyl methacrylate) containing carbonaceous reinforcements—Carbon nanotube, carbon black, and carbon fiber. *J. Plast. Film Sheet.* **2020**, *36*, 409–429. [[CrossRef](#)]
14. Nauman, S. Piezoresistive Sensing Approaches for Structural Health Monitoring of Polymer Composites—A Review. *Eng* **2021**, *2*, 197–226. [[CrossRef](#)]
15. Sethy, D.; Sai, M.; Varghese, F.V.; Balasubramaniam, K. Piezoresistive behaviour of graphene nanoplatelet (GNP)/PMMA spray coated sensors on a polymer matrix composite beam. *eXPRESS Polym. Lett.* **2019**, *13*, 1018–1025. [[CrossRef](#)]
16. Huang, H.; Su, S.; Wu, N.; Wan, H.; Wan, S.; Bi, H.; Sun, L. Graphene-Based Sensors for Human Health Monitoring. *Front. Chem.* **2019**, *7*, 399. [[CrossRef](#)]
17. Sethy, D.; Sai, M.; Varghese, F.V.; Balasubramaniam, K. Passive thermo-elastic behaviour of surface enhanced glass-epoxy composites with spray coated graphene nanoplatelets (GNP). *Mater. Res. Express* **2019**, *6*, 125044. [[CrossRef](#)]
18. Sethy, D.; Sai, M.; Varghese, F.V.; Balasubramaniam, K. Improved Thermal Signature of Composite Beams with GNP Smart Skin for Defect Investigation. *J. Nondestruct. Eval.* **2021**, *40*, 80. [[CrossRef](#)]
19. Balandin, A.A.; Ghosh, S.; Bao, W.; Calizo, I.; Teweldebrhan, D.; Miao, F.; Lau, C.N. Superior Thermal Conductivity of Single-Layer Graphene. *Nano Lett.* **2008**, *8*, 902–907. [[CrossRef](#)] [[PubMed](#)]
20. Freitag, M.; Chiu, H.Y.; Steiner, M.; Perebeinos, V.; Avouris, P. Thermal infrared emission from biased graphene. *Nat. Nanotechnol.* **2010**, *5*, 497–501. [[CrossRef](#)]
21. He, L.; Wang, H.; Zhu, H.; Gu, Y.; Li, X.; Mao, X. Thermal Properties of PEG/Graphene Nanoplatelets (GNPs) Composite Phase Change Materials with Enhanced Thermal Conductivity and Photo-Thermal Performance. *Appl. Sci.* **2018**, *8*, 2613. [[CrossRef](#)]
22. Tsai, M.W.; Chuang, T.H.; Meng, C.Y.; Chang, Y.T.; Lee, S.C. High performance midinfrared narrow-band plasmonic thermal emitter. *Appl. Phys. Lett.* **2006**, *89*, 173116. [[CrossRef](#)]
23. Yao, R.X.; Shi, Z. Steady-State forced vibration of functionally graded piezoelectric beams. *J. Intell. Mater. Syst. Struct.* **2011**, *22*, 769–779. [[CrossRef](#)]
24. Friswell, M.I.; Adhikari, S. Sensor shape design for piezoelectric cantilever beams to harvest vibration energy. *J. Appl. Phys.* **2010**, *108*, 014901. [[CrossRef](#)]
25. Li, P.; You, Z.; Cui, T. Graphene cantilever beams for nano switches. *Appl. Phys. Lett.* **2012**, *101*, 093111. [[CrossRef](#)]
26. Mao, Q. Design of shaped piezoelectric modal sensors for cantilever beams with intermediate support by using differential transformation method. *Appl. Acoust.* **2012**, *73*, 144–149. [[CrossRef](#)]
27. Faniyi, I.O.; Fasakin, O.; Olofinjana, B.; Adekunle, A.S.; Oluwasusi, T.V.; Eleruja, M.A.; Ajayi, E.O.B. The comparative analyses of reduced graphene oxide (RGO) prepared via green, mild and chemical approaches. *SN Appl. Sci.* **2019**, *1*, 1181. [[CrossRef](#)]
28. Lee, H.; Kim, M.J.; Kim, J.H.; Lee, J.Y.; Choi, H.J.; Shim, W.; Lee, G.H. Highly flexible graphene nanoplatelet-polydimethylsiloxane strain sensors with proximity-sensing capability. *Mater. Res. Express* **2020**, *7*, 045603. [[CrossRef](#)]
29. Song, X.; Liu, X.; Peng, Y.; Xu, Z.; Liu, W.; Pang, K.; Wang, J.; Zhong, L.; Yang, Q.; Meng, J. A graphene-coated silk-spandex fabric strain sensor for human movement monitoring and recognition. *Nanotechnology* **2021**, *32*, 215501. [[CrossRef](#)] [[PubMed](#)]
30. Sengupta, D.; Muthuram, V.; Kottapalli, A.G.P. Flexible Graphene-on-PDMS Sensor for Human Motion Monitoring Applications. In Proceedings of the 2020 IEEE SENSORS, Rotterdam, The Netherlands, 25–28 October 2020; pp. 1–4.
31. Wall, J.C.; Turnbull, G. Gait asymmetries in residual hemiplegia. *Arch. Phys. Med. Rehabil.* **1986**, *67*, 550–553. [[PubMed](#)]
32. Fan, Y.; Zhao, H.; Yang, Y.; Yang, Y.; Ren, T.; Tu, H. A Practical Strain Sensor Based on Ecoflex/Overlapping Graphene/Ecoflex Sandwich Structures for Vocal Fold Vibration and Body Motion Monitoring. *Front. Sens.* **2022**, *2*, 815209. [[CrossRef](#)]

33. Arjmadni, N.; Lagae, L.; Borghs, G. Enhanced resolution of poly (methyl methacrylate) electron resist by thermal processing. *J. Vac. Sci. Technol. B Microelectron. Nanometer Struct.* **2009**, *27*, 1915–1918. [[CrossRef](#)]
34. Abbas, W.; Bakr, K.O.; Nassar, M.M.; Abdeen, M.A.M.; Shabrawy, M. Analysis of Tapered Timoshenko and Euler–Bernoulli Beams on an Elastic Foundation with Moving Loads. *J. Math.* **2021**, *2021*, 6616707. [[CrossRef](#)]
35. Demir, C.; Civalek, O.; Akgöz, B. Free Vibration and Bending Analyses of Cantilever Microtubules Based on Nonlocal Continuum Model. *Math. Comput. Appl.* **2010**, *15*, 289–298.
36. Stanley, D. *Surgical Anatomy of the Hand and Upper Extremity*; Doyle, J.R., Botte, M.J., Eds.; Lippincott, Williams & Wilkins: Philadelphia, PA, USA, 2003; Volume 86-B, p. 783.
37. Oliveira, L.F.; Matta, T.T.; Alves, D.S.; Garcia, M.A.C.; Vieira, T.M.M. Effect of the shoulder position on the biceps brachii emg in different dumbbell curls. *J. Sports Sci. Med.* **2009**, *8*, 24–29. [[PubMed](#)]
38. Kirsch, J.M. The Exercise That Heals the Shoulder and Relieves Back Pain. In *Shoulder Pain? The Solution Prevention: Fifth Edition, Revised & Expanded, Fourth Edition, Revised & Expanded*; Bookstand Publishing: Morgan Hill, CA, USA, 2013; p. 50.
39. Sheffler, L.C.; Lattanza, L.; Williamson, M.S.; James, M.A. Biceps brachii long head overactivity associated with elbow flexion contracture in brachial plexus birth palsy. *J. Bone Jt. Surg. Am.* **2012**, *94*, 289–297. [[CrossRef](#)] [[PubMed](#)]
40. Muscolino, J. *The Muscular System Manual—The Skeletal Muscles of the HUMAN Body*, 4th ed.; Elsevier-Health Sciences Division: New York, NY, USA, 2016; ISBN 9780323327718.
41. Oglat, A.A.; Matjafri, M.Z.; Suardi, N.; Oqlat, M.A.; Abdelrahman, M.A.; Oqlat, A.A. A review of medical doppler ultrasonography of blood flow in general and especially in common carotid artery. *J. Med. Ultrasound* **2018**, *26*, 3–13. [[CrossRef](#)] [[PubMed](#)]